Composites Part B 212 (2021) 108713

Contents lists available at ScienceDirect

Composites Part B

journal homepage: www.elsevier.com/locate/compositesb

Zinc-doped silica/polyaniline core/shell nanoparticles towards corrosion protection epoxy nanocomposite coatings

Seyyed Arash Haddadi [a,*], Erfan Mehmandar [b,1], Hossein Jabari [b,1], Ahmad Ramazani S.A. [b], Rahman Mohammadkhani [b], Ning Yan [c,d], Mohammad Arjmand [a,**]

[a] Nanomaterials and Polymer Nanocomposites Laboratory, School of Engineering, University of British Columbia, Kelowna, BC, V1V 1V7, Canada
[b] Chemical and Petroleum Engineering Department, Sharif University of Technology, PO Box 11155-9465, Tehran, Iran
[c] Graduate Department of Forestry, John H. Daniels Faculty of Architecture, Landscape and Design, University of Toronto, 33 Willcocks Street, Toronto, ON M5S 3B3, Canada
[d] Department of Chemical Engineering & Applied Chemistry, University of Toronto, 200 College Street, Toronto, ON, M5S 3E5, Canada

ARTICLE INFO

Keywords:
Mesoporous silica
Polyaniline
Epoxy
pH triggered release
Barrier/active protection

ABSTRACT

Commercial paints and coatings can serve as a protective barrier for metallic substrates in a corrosive environment. A considerable variety of nanostructures can be embedded in a polymeric coating to achieve both barrier and active protection. This research aims to elucidate the role of polyaniline (PANI) as an active polyelectrolyte modifier for the surface modification of mesoporous silica nanoparticles (MSNs) doped with zinc cations (Zn^{2+}). To characterize the samples, we employed different techniques, including field-emission scanning electron microscopy (FE-SEM), transmission electron microscopy (TEM), N_2 adsorption-desorption, Fourier transform infrared spectroscopy (FTIR), Raman spectroscopy, X-ray diffraction (XRD), thermogravimetric analysis (TGA), inductively coupled plasma optical emission spectroscopy (ICP-OES), rheometric mechanical spectroscopy (RMS), differential scanning calorimetry (DSC), tensile, and electrochemical impedance spectroscopy (EIS). Characterization of PANI-MSNs proved the formation of PANI shells onto the surface of silica cores, and pH triggered the release of Zn^{2+} at the alkaline condition. Enhancement in rheological, thermal, and mechanical characteristics revealed good dispersion and chemical interaction between PANI coated nanoparticles and the epoxy matrix. Moreover, epoxy nanocomposite coatings illustrated a dual barrier/active protection after 50 days of salt immersion.

1. Introduction

In the wake of the proliferation of different industrial production infrastructures, such as petrochemicals, agricultural, automotive, and marine and shipyards, across the world, corrosion protection of metallic objects such as vessels, pipes, and main bodies of instruments has become a matter of concern for the corresponding industries [1–3]. Small and large industrial units worldwide pay voluminous and rising costs to compensate for the damages and detriments caused by corrosion [4–6]. Among various approaches to control and protect metals against corrosion, polymeric coatings and paints have held great stand due to low cost, low energy consumption, short inspection time, and superior durability and efficiency [7,8]. Nevertheless, insufficient corrosion resistance of commercial coatings and paints is yet an unsolved challenge for the industry [8,9].

Commercial coatings and paints, such as epoxy, can provide an intact and defect-free protective layer onto the surface of metals for a short period of time. With increasing exposure time, the corrosive electrolyte can penetrate through the coating, reach the metal/coating interface, and disband the coating from the metallic substrate [10,11]. Incorporation of additives, such as corrosion inhibitors, pigments, and micro/-nanostructures, into the coating can prevent the formation of micropores, voids, and defects in a coating and increase the tortuous path of the electrolyte to reach the metal/coating interface [12,13]. Over the last decade, many attempts have been extensively made to enhance the corrosion protection performance (CPP) of coatings by

* Corresponding author.
** Corresponding author.
E-mail addresses: seyyedarash.haddadi@ubc.ca (S.A. Haddadi), mohammad.arjmand@ubc.ca (M. Arjmand).
[1] Erfan Mehmandar and Hossein Jabari contributed equally to this work.

https://doi.org/10.1016/j.compositesb.2021.108713
Received 7 October 2020; Received in revised form 2 February 2021; Accepted 6 February 2021
Available online 10 February 2021
1359-8368/

introduction of a wide range of nanoparticles, such as ZnO [14], Ag_2O [15], ZrO_2 [16], clay [17], SiO_2 [18], Fe_2O_3 [19], MoS_2 [20], Zeolite [21], halloysite [22], CNT [23], and graphene [24,25]. Nanoparticles, due to their large specific surface area, can remarkably promote barrier properties of coatings against the penetration of aggressive species, like water, oxygen, and chloride ions inside [26,27]. Among different types of porous and mesoporous nanostructures, MSNs have attracted a great deal of attention as a good host for the encapsulation of corrosion inhibitors due to the large specific surface area (700–1500 $m^2\ g^{-1}$), and high thermal and chemical stability. There is abundant hexagonal packing of pores with a uniform cylindrical structure on the surface of MSNs with a diameter range of 2–50 nm [28,29].

Porous nanoparticles, such as SiO_2, CeO_2, and carbon hollow spheres due to the existence of nanopores and cavities in their structures, cannot provide good barrier properties for long-term exposure times [3,11,30]. In fact, these nanopores and cavities can act as nanoscopic reservoirs for electrolyte accumulation, leading to gradual deterioration and delamination of the coatings from metallic substrates. However, due to the negative effects associated with the direct loading of corrosion inhibitors on the curing kinetics of the coatings and some unwanted chemical interactions with other components, nanopores and cavities of mesoporous nanostructures are highly desirable to store corrosion inhibitors instead [31–33]. On-demand release of corrosion inhibitors under certain stimulations, such as pH, UV-radiation, thermal chock, or temperature change, can be achieved through a corrosion-inhibitor-doped assembly featuring polyelectrolyte layer as the shell and mesoporous nanoparticle as the core [34–36]. The release of corrosion inhibitors under specific stimulations from the mesoporous cores is tuned based on the properties of the polyelectrolyte shell, which acts as the gatekeeper [37,38]. Yeganeh et al. [29] used functionalized MSNs loaded with molybdate ion (MSInh) as the corrosion inhibitor in a polypyrrole matrix. Results showed that in the presence of loaded MSInh, better active corrosion protection was observed for steel substrates due to the formation of protective compounds after the release of MSInh from MSNs at the steel/polypyrrole interface. In another work conducted by Yeganeh et al. [39] sulfamethazine, as a corrosion inhibitor, was loaded in MSNs to fabricate corrosion protective epoxy nanocomposite coatings. Results revealed remarkable enhancements in barrier properties and active corrosion performance of the epoxy coating in the presence of 1 wt % sulfamethazine loaded MSNs.

Polyaniline and polypyrrole, as a well-known class of intrinsically conducting polymers, are widely used for the functionalization of micro/nanoparticles and the construction of core/shell structures. Surface functionalization of nanoparticles, such as graphene oxide, by polyaniline, enhances electrical, mechanical, and corrosion protective properties of corrosion protection coatings. Polyaniline, due to its excellent properties, i.e., low cost, environmental stability, being an anodic inhibitor, and facile synthesis method (oxidative polymerization), can be introduced as a good candidate for the functionalization of nanoparticles to make corrosion inhibitors loaded core/shell nanostructures [40–42].

As reported previously, polyaniline has been used for the fabrication of a polyelectrolyte shell via layer-by-layer (L-b-L) assembly strategy followed by in-situ polymerization onto the surface of some nanoparticles [38,43]. Electrochemical results demonstrated that barrier properties and active corrosion performance of coatings were enhanced in the presence of the polyaniline shells. Moreover, several publications explored polyaniline as an anodic corrosion inhibitor as it can release nitrate anions, blocking the anodic corrosion reactions through the creation of passive layers on active sites in metallic substrates [35]. Some research studies claimed that polyaniline doped with ecofriendly cations, such as cerium (Ce^{3+}) and zinc (Zn^{2+}) as green corrosion inhibitors, illustrated both anodic/cathodic corrosion inhibition properties, named as mixed-type, in corrosive solutions for mild steel [35,38,44].

In this research, mesoporous silica nanoparticles were synthesized based on the Stober method using a surfactant as the template [45–47]. Mesoporous silica nanoparticles (MSN), due to their low cost, excellent chemical and thermal stability, simple synthesis procedure with tunable physical shape, size, and surface characteristics, were used as the solid core. Positively charged polyaniline layers were grafted as polyelectrolyte shells on the surface of the mesoporous silica nanoparticles by the in-situ polymerization in the presence of zinc cations. Mesoporous silica/polyaniline core/shell assembly (PANI-MSN) were characterized using FE-SEM, TEM, FT-IR, Raman, XRD, and UV–visible analyses. Kinetic release of zinc cations from the core/shell nanoparticles in the saline solution as a function of time at different pH values was studied using ICP-OES. Epoxy nanocomposite coatings were fabricated by incorporation of 3 wt % MSNs and PANI-MSNs, respectively. The rheological, mechanical, thermal, and electrochemical properties of the prepared nanocomposites were investigated by RMS, tensile test, DSC, and EIS, respectively, and results are discussed in relation to their structural and compositional characteristics.

Table 1
Elemental composition of ST37 mild steel panels.

Element	S	Mn	C	Si	P	Fe
wt. %	0.05	0.5	0.12	0.3	0.045	balance

2. Experimental

2.1. Chemicals

Absolute ethanol (95%, USA) and methanol (99.8%, USA), acetone (≥99.5%, USA), tetraethyl orthosilicate (TEOS, $Si(OC_2H_5)_4$, 98%, Germany), aqueous ammonia (28 wt %, NH_3, USA), cetyltrimethylammonium bromide (CTAB, $CH_3(CH_2)_{15}N(Br)(CH_3)_3$, ≥99%, Germany), aniline monomer (≥99.5%, Germany), hydrochloric acid (37 wt %, HCl, USA), nitric acid (HNO_3, 70%, USA), ammonium persulphate (APS, $(NH_4)_2S_2O_8$, ≥98%, Germany), sodium chloride (NaCl, ≥ 99%, USA), and zinc nitrate ($Zn(NO_3)_2$, 98%, Germany) were purchased from Sigma-Aldrich, and used as received. High solid epoxy resin (Epikote 828) and polyamine hardener (Epikure F205) were precured from Kian Resin Co., Iran. Mild steel panels (ST37, 10 × 8 × 0.15 cm^3), as substrates, were obtained from Foolad Mobarakeh Co., Iran, used for electrochemical measurements with the elemental composition tabulated in Table 1.

2.2. Synthesis of the MSN cores

MSNs, as cores, were synthesized in accordance with the Stober method using a hard-templating method [45–47]. A round-bottom flask of 500 mL containing DI water (160 mL) and CTAB (1 g), as the template, was used as the synthesis medium. Then, aqueous ammonia (5 mL) as the reaction catalyst was added into the mixture under stirring (300 rpm). In an Erlenmeyer flask of 50 mL, TEOS (5 mL) was dissolved completely in ethanol (25 mL). Next, the TEOS/ethanol solution was added drop-by-drop to the solution made earlier under stirring (300 rpm). The homogeneous white suspension of MSN in the water/ethanol solution was obtained after 3 h at 30 °C. Colloidal nanoparticles were collected using centrifugation and washed with ethanol/water mixture (4:1 v/v). The precipitation was transferred to a round-bottom flask of 500 mL connected to a distillation column containing ethanol (120 mL) and HCl (4 mL) to remove CTAB templates at 75 °C for 4 h. The template removal process was repeated 5 times to ensure the complete extraction of CTAB templates. Finally, prepared MSNs were dispersed in DI water for the next steps.

2.3. Synthesis of MSN/PANI core/shell nanostructures

Grafting of PANI as polyelectrolyte shells on the surface of MSNs was

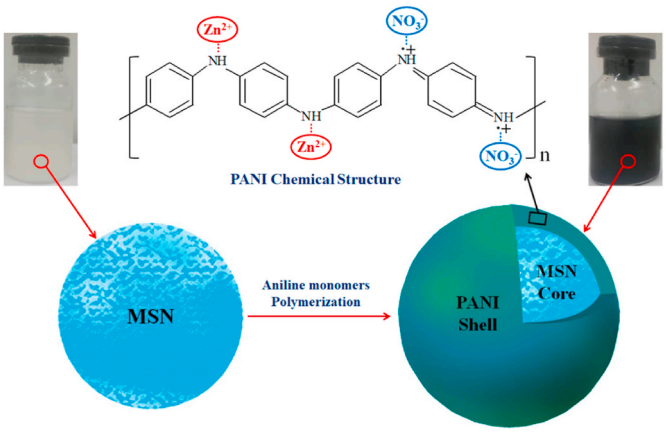

Fig. 1. Schematic illustration of the synthesis procedure of the MSN/PANI core/shell nanostructures.

performed based on the in-situ polymerization of aniline monomers [38, 42]. For this purpose, 20 mL of DI water containing 5 mL of HNO_3, MSNs (0.2 g), and $ZnCl_2$ (1 g L^{-1}) was transferred to a round-bottom flask of 50 mL, then 2 mL of polyaniline was added, and the mixture was placed in a bath sonication (120 W, 37 kHz, Elma Co.) at 1–3 °C. In a second container, APS (1.2 g) was dissolved in DI water at 2–5 °C, and then added instantly to the previous solution. After 30 min of sonication, the mixture was kept in a fridge at 2–5 °C for 24 h. Finally, the product was filtered by centrifugation, washed 3 times with DI water, and 2 times with methanol, alternatively, and suspended in methanol to avoid agglomeration. Fig. 1 shows the schematic illustration of the synthesis procedure of the MSN/PANI core/shell nanostructures.

2.4. Samples preparation

Before the preparation of epoxy nanocomposite coatings, a wet transfer method (WTM) was employed to add separately 3 wt % of MSNs and PANI-MSNs in the epoxy resin. The obtained compounds were mixed using a high-speed mixer (4000 rpm) for 30 min, and a probe sonicator (150 W, 37 kHz, Adeeco Co.) for 5 min to disperse MSNs and PANI-MSNs uniformly in the matrix. Mild steel panels were abraded using sandpapers (grades 400, 600, and 1000), and degreased with acetone to remove all organic impurities. MSNs and PANI-MSNs loaded epoxy coatings were blended with polyamine hardener in a stoichiometric ratio of 2:1 w/w. Then, epoxy coatings without and with MSNs and PANI-MSNs were applied on the surface of mild steel plates using a four-side film applicator with a wet thickness of 90 μm. All coated panels were kept at ambient conditions for 24 h, and then post-cured for 1 h in an oven at 100 °C. The epoxy coating containing no MSNs and PANI-MSNs (EP) was used as the control sample. For electrochemical measurements, an area of 1 × 1 cm^2 was used as a test area for intact coatings, while for scratched coatings, an area of 2 × 2 cm^2 with a forged scratch (8 mm in length and 25 ± 10 μm in width) in the middle was selected. The remaining area of each panel was covered with a hot mixture of beeswax-colophony (3:1.2 w/w). Extract solutions containing 3.5 wt % NaCl were prepared for the visual assessment of uncoated metallic panels. The procedure of extract solutions preparation is explained in supporting information (SI), Section 1.

2.5. Techniques

2.5.1. PANI-MSN characterization

A Mira TESCAN FE-SEM analyzer (3-XMU, Czech Republic) was utilized to evaluate morphological properties, shape, and particle size of synthesized MSNs and PANI-MSNs, and the morphology of metallic surfaces. Energy-dispersive X-ray spectroscopy (EDX, Oxford Instruments, United Kingdom) was employed for the elemental characterization of the scratched region of the coatings. Brunauer-Emmett-Teller (BET) and Barrett-Joyner-Halenda (BJH) methods were employed using a BEL analyzer (BELSORP-miniII, Japan) to determine structural characteristics of MSNs and PANI-MSNs, such as specific surface area, specific volume, pore-volume, and mean pore size. The surface chemistry, chemical bonds of MSNs and PANI-MSNs and nature of grafted PANI shells onto the surface of MSN were examined by a Brucker FTIR spectrometer (Tensor 27, Germany) within the wavenumber range of 4000–400 cm^{-1}. Raman spectra of MSNs and PANI-MSNs were obtained using a Firstguard Raman spectrometer (Rigaku, Japan) at a Raman shift region of 300–2100 cm^{-1}. The crystalline structures of MSNs and PANI-MSNs were assessed using XRD analysis (X-pert Philips, PW 3040/60, The Netherlands) with a graphite monochromator and copper anode, Cu-Kα1 radiation (λ = 1.54 Å), at 40 kV and 20 mA accelerating voltage and current, respectively. The scanning rate of 0.5° min^{-1} was selected at the 2θ range of 5–75° for XRD analyses. The amount of PANI grafted onto the surface of MSNs was determined by means of TGA within a temperature range of 35–550 °C and a heating rate of 10 °C min^{-1} in a nitrogen atmosphere. Further characterization of PANI-MSNs was done by UV–visible spectroscopy (Perkin-Elmer instrument, Lambda 25, USA), explained in detail in SI, Section 2.

2.5.2. Release of Zn^{2+} at different pHs

The release of Zn^{2+} from PANI-MSN core/shell nanostructures at different pH was investigated using a Spectro Arcos ICP-OES spectrometer (Ametec, Germany) at selected periods of time. For this purpose, 3.5 wt % NaCl solutions (pH ~7) were prepared at different pH, HCl (1 M) and NaOH (1 M) solutions were used to adjust pH at ~3 and ~11, respectively. Then, PANI-MSN core/shell nanostructures were dispersed in the test solutions using the bath sonicator with a concentration of 1 g L^{-1}. To establish an equilibrium condition, all test solutions were kept under stirring (500 rpm) for 72 h at ambient conditions. The Zn^{2+} concentration at certain fractions of exposure time was determined using ICP-OES analysis. To clarify the reproducibility of results, all measurements were repeated 3 times.

2.5.3. Characterization of epoxy nanocomposite coatings

Effects of MSNs and PANI-MSNs on the steady viscosity and shear stress behaviour of epoxy coatings before the addition of polyamine hardener were investigated using RMS (Anton Paar, Physica MCR 301, Austria). All measurements were performed in a parallel plate geometry with a gap distance of 0.8 mm at 25 ± 1 °C and 20 ± 5 RH. Effects of MSNs and PANI-MSNs on mechanical properties of epoxy coatings, such as tensile strength, tensile extension, Young's modulus, and toughness, were investigated utilizing a Zwick universal tensile machine (Roell-Z010, Germany) within a tensile rate of 0.5 mm min^{-1} at 25 ± 1 °C and 20 ± 5 RH based on ASTM D638 standard. More details and results related to RMS and tensile tests are provided in detail in SI, Section 3.

CPP of epoxy coatings in the presence and absence of a forged scratch defect was evaluated using EIS test by an AUTOLAB potentiostat (M204, The Netherlands). For this purpose, all mild steel specimens coated with epoxy coatings were dipped in 3.5 wt % NaCl solution at different immersion times. All EIS measurements were performed by means of a three-electrode electrochemical cell including Ag/AgCl electrode (reference electrode), platinum electrode (counter electrode), and mild steel specimens (working electrode) within a frequency region of 0.01–10^4 Hz, and 10 mV peak to peak amplitude at open circuit potential (OCP). All EIS data were analyzed using Z-view software. A salt spray test was carried out to evaluate the CPP of epoxy coatings visually according to ASTM B117 standard at 38 °C, pH 6.5–7, and the NaCl concentration of 5 wt %.

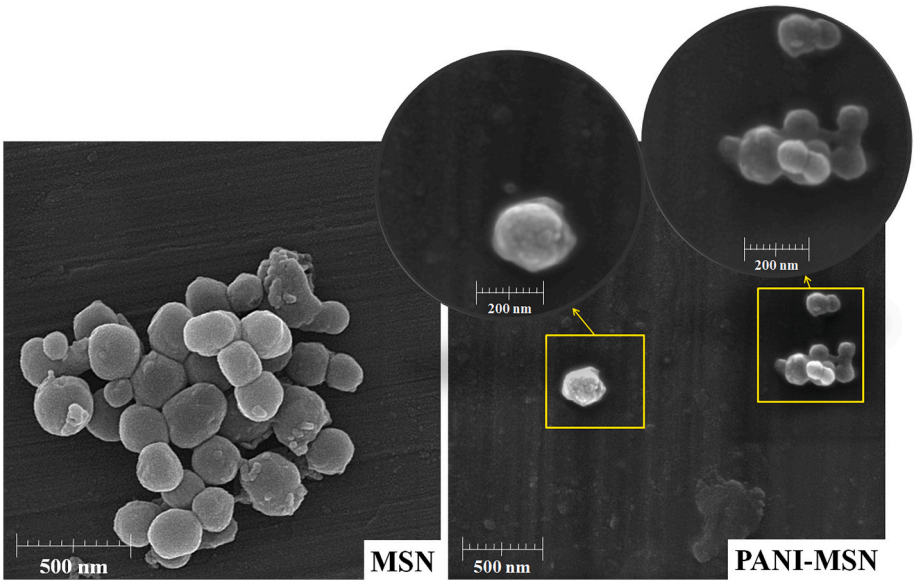

Fig. 2. FE-SEM image of synthesized MSN and PANI-MSN.

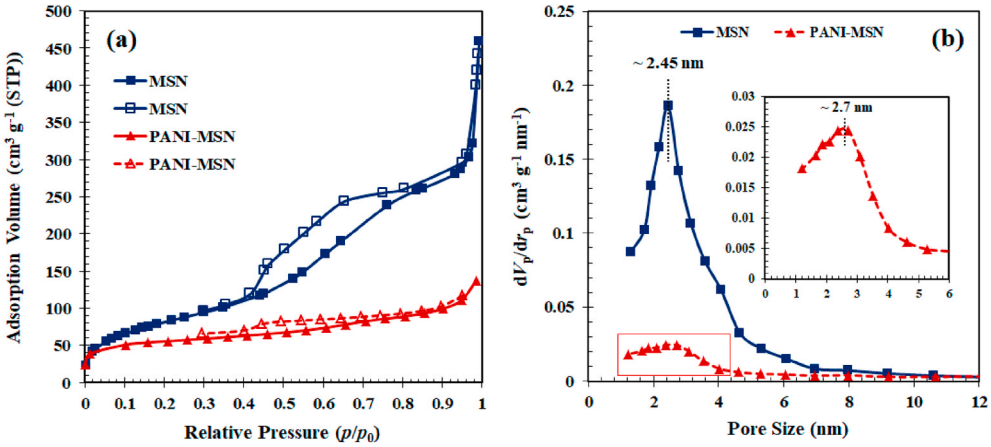

Fig. 3. N_2 adsorption-desorption isotherms and pore size distributions for MSNs and PANI-MSNs.

Table 2
BET parameters obtained from N_2 adsorption-desorption isotherms for MSNs and PANI-MSNs.

Sample	Specific surface area (a_s)/m^2 g^{-1}	Specific volume (V_m)/ cm^3 g^{-1}	Total pore volume/cm^3 g^{-1}	Mean pore diameter/nm
MSN	302	69.43	0.67	8.9
PANI-MSN	192.6	44.2	0.21	4.4

3. Results and discussion

3.1. PANI-MSN characterization

3.1.1. FE-SEM and TEM

The morphology and particle size of synthesized MSN cores before and after grafting of polyaniline polyelectrolyte shells were analyzed using FE-SEM, illustrated in Fig. 2. As shown in Fig. 2a and b, MSNs and PANI-MSNs feature a spherical shape with an average size of ~150 and 250 nm, respectively. Fig. 2b reveals an increase in the dimension of MSN cores after the deposition of polyaniline shells. MSN cores and PANI-MSNs have a lumpy surface due to the presence of mesoporous patterns and the deposition of polyaniline shells on the surface of MSNs, respectively.

3.1.2. BET

The N_2 adsorption-desorption isotherms of MSNs and PANI-MSNs were assessed using the BET method to obtain the BET features in the absence and presence of polyaniline shells. The N_2 adsorption-desorption isotherms, pore size distribution, and summarized BET parameters are presented in Fig. 3 and Table 2, respectively. As illustrated in Fig. 3a, an H3-type hysteresis loop placed in a 0.4–0.95 relative pressure for the IV-shaped IUPAC isotherm of MSNs proves the mesoporous structure for MSNs. Also, the deposition of polyaniline shells on the surface of MSNs altered the type of hysteresis loop from H3 to H4. H4 type of hysteresis loops appears in nanostructures with a composite nature, such as activated carbons and decorated nanoparticles with polymers and/or other nanoparticles [48]. Through the polymerization of polyaniline monomers, a portion of reactive agents (monomer, initiator, etc.) can penetrate into the nanoporous cavities of MSNs, polymerize, and heap these cavities. In fact, the blockage of pores and cavities and covering the surface of MSNs with polyaniline account for the significant decrement of a_s, V_m, and total pore volume from 309, 69.4, and 0.67–193 m^2 g^{-1}, 44.2 cm^3 g^{-1}, and 0.21 cm^3 g^{-1},

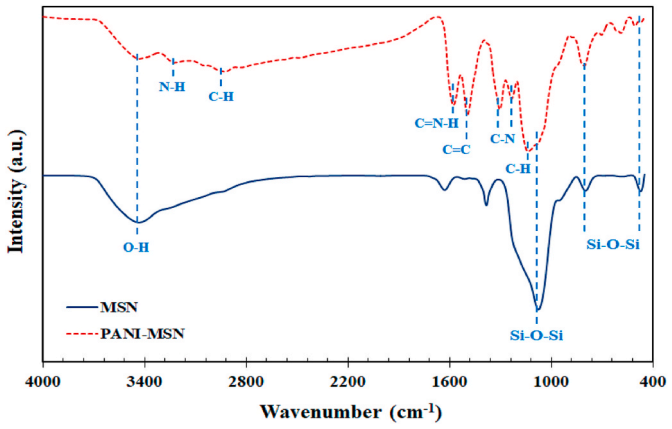

Fig. 4. FTIR spectra of synthesized MSNs and PANI-MSNs.

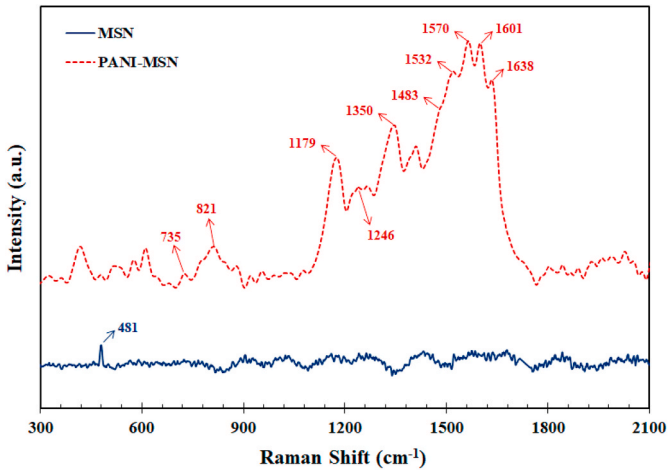

Fig. 5. Raman spectra of MSNs and PANI-MSNs.

respectively. Moreover, the mean pore diameter of MSNs after the deposition of polyaniline declined from 8.9 to 4.4 nm. The pore size distribution obtained by BJH method, shown in Fig. 3b, for MSNs has a peak centered at 2.45 nm, while by the deposition of polyaniline on the surface of MSNs, this peak shifted to 2.7 nm with a lower intensity, demonstrating the formation of uniform polyaniline shells on the surface of MSNs. This observation is in line with the obtained FE-SEM and TEM results.

3.1.3. FTIR

The chemical bonds of MSNs before and after the deposition of polyaniline shells were studied utilizing FTIR analysis. FTIR spectra of MSNs and PANI-MSNs are demonstrated in Fig. 4. As shown in Fig. 4, the FTIR spectrum of MSNs presents different transmittance peaks, including vibration of O–H bond (~3476 cm^{-1}), Si–O–Si asymmetric stretching (~491 and ~1094 cm^{-1}), and Si–O–Si network (~806 cm^{-1}) [34,49]. After the formation of polyaniline shells, some new peaks appeared in the FTIR spectrum of PANI-MSNs. The peaks that appeared at ~3247 and ~2948 cm^{-1} are assigned to the N–H stretching

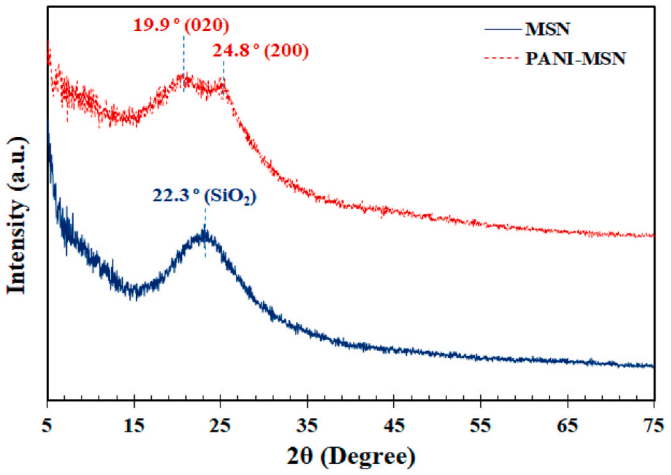

Fig. 6. XRD patterns of MSNs before and after grafting of PANI shells.

vibration of the secondary amine groups and emeraldine base and C–H asymmetric stretching in PANI chains, respectively [30,44]. Stretching of C═N–H, C═C vibration in quinoid rings, and C–N vibration of aromatic amines appeared at ~1590 cm^{-1}, ~1504 cm^{-1}, ~1246 and ~1314 cm^{-1}, respectively [49–51]. The shoulder peak overlapped with the asymmetric stretching of Si–O–Si is assigned to C–H wagging in PANI chains [49,51]. FTIR results clearly proved the successful deposition of PANI shells on the surface of MSNs.

3.1.4. Raman spectroscopy

Raman spectroscopy was employed for further characterization of MSNs and PANI-MSNs to assess the chemical interactions between MSN cores and PANI shells. Raman spectra and main characteristic peaks of MSNs and PANI-MSNs are shown in Fig. 5 and Table 3. According to Fig. 5, in the Raman spectrum of MSNs, only one characteristic peak can be observed at ~481 cm^{-1}, related to torsional vibrations and bending modes of O–Si–O bond [49,52]. By grafting of PANI shells on the surface of MSNs, various characteristic peaks appeared in the Raman spectrum of PANI-MSNs, illustrated in Fig. 5 and Table 3, corroborating the formation of PANI on the surface of MSNs. Among these peaks, the peak located at 1350 cm^{-1} is assigned to stretching vibrations of C~N^+ intermediate bonds [49,53]. In addition, the peak centered at 735 and 821 cm^{-1} are related to the deformation vibrations of quinine rings and amine groups of PANI chains [53,54]. Raman spectroscopy results are in line with those of the FTIR analysis.

3.1.5. XRD

The crystalline structures of MSNs before and after grafting of PANI shells were evaluated using the XRD technique. As shown in Fig. 6, a broad diffraction peak at $2\theta = 22.3°$ is related to the amorphous structure of MSNs [34,55]. The appearance of new characteristics wide peaks at $2\theta = 10–30°$ in the pattern of PANI-MSNs is linked to PANI chains grafted on the surface of MSNs. The diffraction peaks located at $2\theta = 19.9°$ and $2\theta = 24.8°$ are assigned to the parallel and perpendicular periodicity of PANI chains [56,57]. These two broad peaks in the diffraction pattern of PANI-MSNs demonstrate the low crystallinity of PANI due to the quinoid and benzenoid rings repetition in PANI chains.

Table 3
Main characteristic peaks appeared in the Raman spectra of MSNs and PANI-MSNs [49,53,54].

Sample	Raman Shift (cm^{-1})							
	C–C	C=C	C–H	€N^+	C–N	C=N	N–H	O–Si–O
MSN	–	–	–	–	–	–	–	481
PANI-MSN	1601	1638, 1570	1179	1350	1246	1483	1532	–

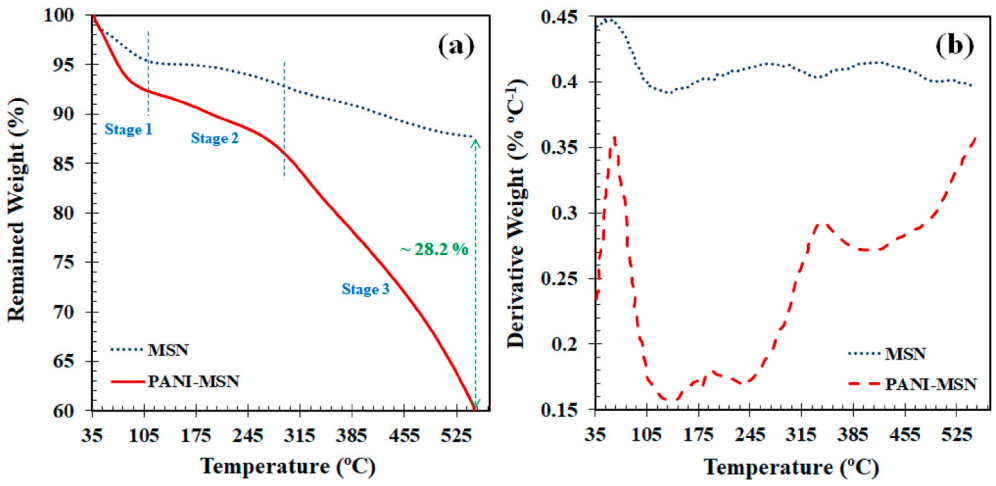

Fig. 7. TGA (a) and DTG (b) thermograms of MSNs and PANI-MSNs.

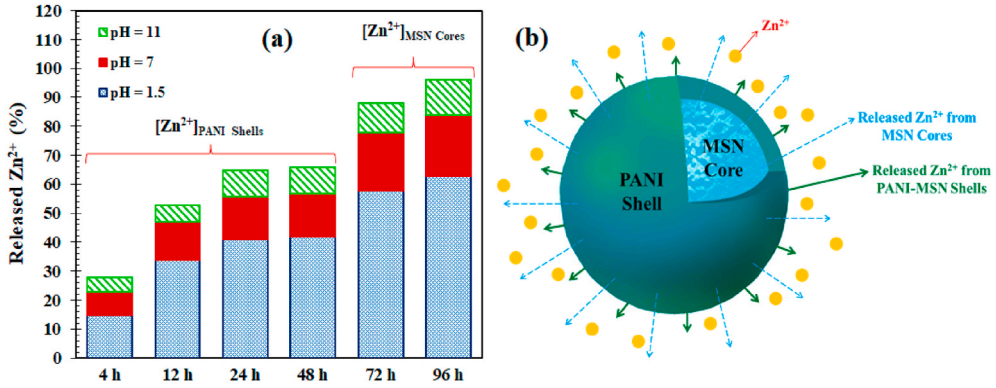

Fig. 8. Zn^{2+} release kinetics as a function of the time at different pHs (a) and schematic illustration of Zn^{2+} release from PANI-MSNs (b).

3.1.6. TGA

Thermal stability and the ash content of MSNs and PANI-MSNs were assessed using TGA-DTG analysis, shown in Fig. 7a and b. Three different stages of weight loss can be observed for MSNs and PANI-MSNs. The dehydration of water molecules adsorbed onto the surface of nanoparticles occurred at 35–105 °C. The final weight loss of 7.8% for MSNs at stages two and three is related to the thermal decomposition of CTAB molecules and unreacted TEOS encapsulated in the internal spaces, and the formation of siloxane bridges, due to the dehydration of internal silanol groups. The significant weight loss of PANI-MSNs around 32% at 105–550 °C is mainly linked to the thermal degradation of unreacted monomers, CTAB molecules, and PANI chains grafted on the surface of MSNs [58]. At 550 °C, the difference between the ash content of MSNs and PANI-MSNs, which is around 28.2%, originates from the presence of PANI shells. These observations prove the grafting of PANI chains onto the surface of MSNs, which is in good agreement with the BET, FTIR, Raman, and XRD results.

3.2. pH triggered release of Zn^{2+} from PANI-MSN

The effects of pH on the release of Zn^{2+} from PANI-MSNs were studied using ICP-OES technique as a function of time, illustrated in Fig. 8a. As depicted in Fig. 8a, the lowest concentrations of released Zn^{2+} were detected at pH 11. Haddadi et al. [34] presented that silica nanoparticles have a negative surface charge, which is responsible for the formation of attractive forces between zinc cations and the surface of mesoporous silica cores. Also, released Zn^{2+} cations could react with hydroxyl groups present in the alkaline solution (pH 11) and form insoluble zinc hydroxide precipitates. Thus, in the alkaline conditions, less amount of released Zn^{2+} cations were detected by ICP-OES. By the decrement of pH from 11 to 7 and 7 to 1.5, the concentration of Zn^{2+} increased with elapsing time, which might be due to the protonation of N–H groups of polyaniline chains in the acidic conditions. In this state, Zinc-PANI complexes can break, and physically adsorbed Zn^{2+} cations can be released from polyaniline chains and the surface of MSNs, respectively, as a result of the repulsive forces. Moreover, the pH can control the ion transportation capability of the conducting polymers [59,60]. In the alkaline solutions (pH >> 7), the hydrophilic characteristics of PANI chains increase, encouraging the diffusion and transportation of Zn^{2+} from PANI shells to the host solution [61]. The shifting of the released Zn^{2+} concentration to the higher value after 48 h might be due to the release of Zn^{2+} encapsulated in the mesoporous medium of MSN cores, shown schematically in Fig. 8b. It seems that pH-sensitive properties of zinc-PANI complexes are responsible for the pH triggered the release of Zn^{2+} from PANI-MSN. Visual assessment was conducted on uncoated metallic panels to evaluate the effects of MSNs and PANI-MSNs extracts on the appearance of uncoated panels after immersion in the corrosive test solutions. More details and interpretations are provided in SI, Section 4.

3.3. Electrochemical investigation of coatings

3.3.1. Epoxy coatings with a forged scratch

The active CPP of the epoxy coatings with a forged scratch was studied using the EIS test. Nyquist and Bode diagrams of the scratched epoxy coatings after immersion in 3.5 wt % NaCl solution at different

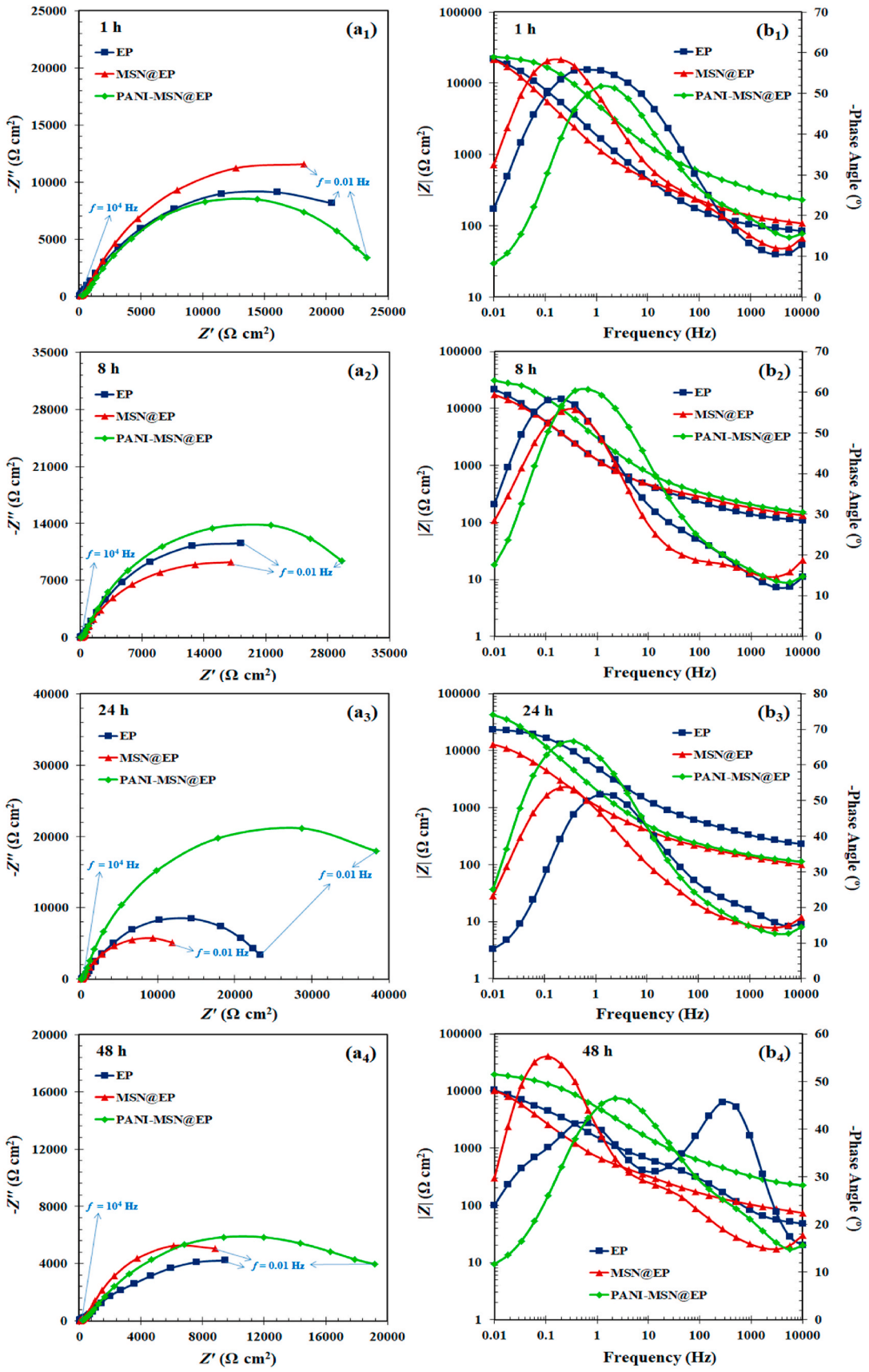

Fig. 9. Nyquist ((a_1)-(a_4)) and Bode ((b_1)-(b_4)) plots of epoxy coatings in the presence of a forged scratch dipped in 3.5 wt % NaCl solution at different immersion times.

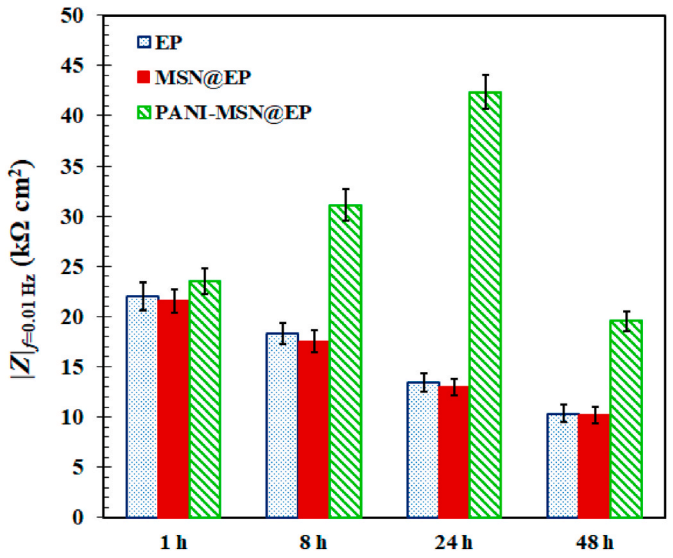

Fig. 10. $|Z|_{f=0.01\ Hz}$ values obtained from Bode plots for epoxy coatings at different immersion times.

times are depicted in Fig. 9. The diameter of semicircles in Nyquist diagrams can be determined as an indicator for the comparison of the overall CPP of coatings. As expected, for EP and MSN@EP coatings, a descending trend was observed for the diameter of semicircles in Nyquist diagrams, total resistance, and impedance in Nyquist and Bode diagrams with no active CPP. That is why EP and MSN@EP coatings presented the same $|Z|_{f=0.01\ Hz}$ values at all immersion times. The reason behind this observation can be attributed to the penetration of the corrosive electrolyte and the development of corrosion reactions at the metal/coating interface in the scratch, resulting in the delamination and deterioration of the coatings at longer immersion times. As can be seen in phase diagrams (Fig. 9b_1–9b_3), the appearance of the second time constant can be assigned to the formation of corrosion products on the metal/coating interface in the scratch.

For a better understanding of the active CPP, values of the impedance modulus at the lowest frequency ($|Z|_{f=0.01\ Hz}$) are presented in Fig. 10. For PANI-MSN@EP coating, $|Z|_{f=0.01\ Hz}$ value shifted from 23.5 to 42.3 kΩ cm^2 after 24 h immersion in the electrolyte. The upward trend of $|Z|_{f=0.01\ Hz}$ for PANI-MSN@EP coating is linked to the active CPP of the coating in the presence of doped Zn^{2+} and polyaniline shells. When the immersion time elapses, Zn^{2+} cations can release in the scratch region, react with hydroxyl groups generated by the cathodic reactions ($2H_2O + O_2 + 4e^- \rightarrow 4OH^-$), and form insoluble zinc hydroxyl ($Zn(OH)_2$) depositing on the cathodic sites, as illustrated schematically in Fig. 11.

Based on the literature [44,62], in the presence of PANI, Fe^{2+} generated by the anodic reactions ($Fe \rightarrow Fe^{2+} + 2e^-$) can be turned to a stable oxidized form (Fe_2O_3), forming a dense passive layer on the anodic sites. Also, the emeraldine salt form of PANI might be oxidized on the surface of the metallic substrate and turn to the leuco-emeraldine form. It seems that at a longer immersion time (48 h), formed protecting layers on the active sites of the metallic substrates became more permeable, and the development of the corrosion products and corroded sites resulted in a decrease in $|Z|_{f=0.01\ Hz}$. In conclusion, EIS measurements for the scratch coatings exhibited that the release of Zn^{2+} cations accompanied by the presence of PANI as shells for MSNs can form a

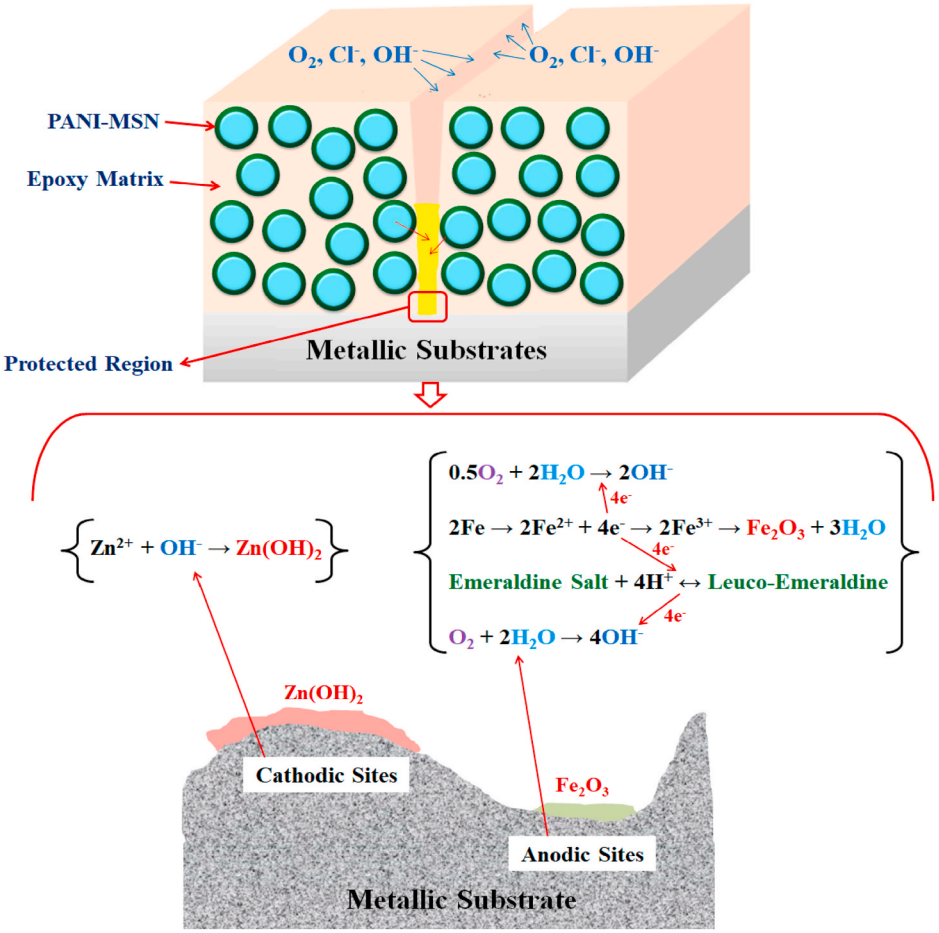

Fig. 11. Inhibition reaction scheme for PANI-MSN@EP coating.

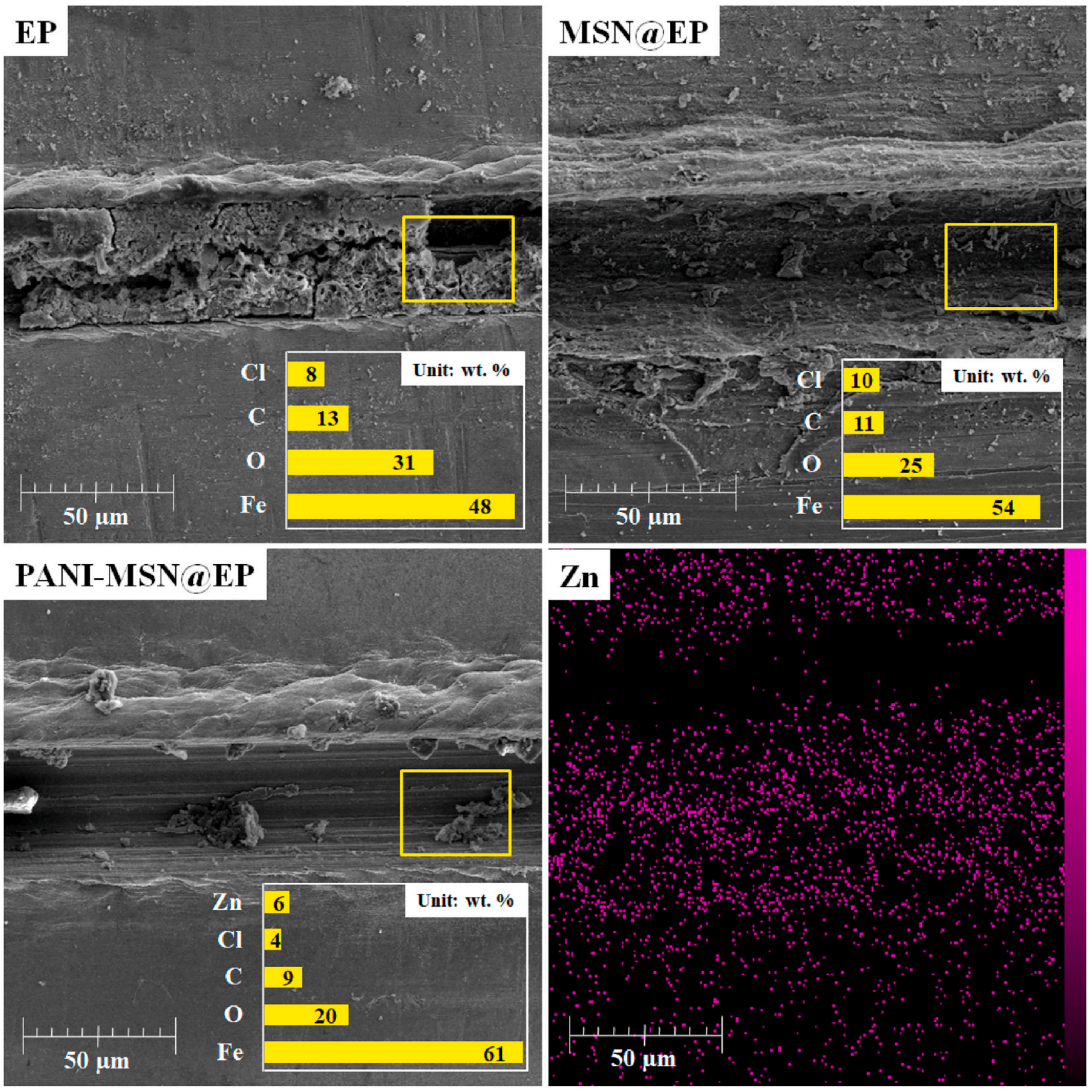

Fig. 12. FE-SEM images of the scratched region for different epoxy coatings after 48 h immersion in the corrosive electrolyte and the elemental mapping of Zn for the scratch region of PANI-MSN@EP.

passive layer in the scratch region and protect the metallic substrate against the destructive corrosion reactions.

FE-SEM and EDS-elemental mapping analyses were conducted on the scratched regions for different epoxy coatings after the coating detachment, shown in Fig. 12. As can be seen, for EP and MSN@EP coatings with no active CPP, rusts and other corrosion products were formed inside the scratch due to the development of corrosion reactions, whereas fewer corrosion products were seen for PANI-MSN@EP coating. Higher contents of O detected via EDX for EP (31 wt %) and MSN@EP (25 wt %) coatings than that of PANI-MSN@EP (20 wt %), related to the larger amount of generated corrosion products inside the scratch. Larger contents of Fe (61 wt %), smaller content of Cl (4 wt %), and detection of Zn (6 wt %) in the scratched region of PANI-MSN@EP coating compared to other coatings are clear pieces of evidence for the release of Zn^{2+} from PANI-MSNs and formation of the passive protective layer inside the scratch. The mapping and detection of Zn in the scratch region of PANI-MSN@EP coating demonstrate the release of Zn^{2+} from PANI-MSNs containers and the formation of Zn-based protective compounds inside the scratch.

3.3.2. Intact epoxy coatings

As stated in Section 3.3.3.1, the active CPP of scratched epoxy coatings was examined, and the epoxy coating containing PANI-MSNs showed an active CPP for short periods of time. The barrier properties and long-term CPP of intact epoxy coatings were also investigated using the EIS test. Fig. 13 displays the Nyquist and Bode diagrams of different epoxy coatings at various times of immersion in 3.5 wt % NaCl solution. To extract electrochemical parameters from the impedance data, all EIS diagrams were fitted by proper equivalent electrical circuits (EECs), including one-time constant (R(RQ)) and two-time constants (R(RQ (RQ))) models. As depicted in Fig. 13, in these EECs, solution resistance, coating resistance, charge transfer resistance, constant phase element of coating, and double layer are presented by R_s, R_c, R_{ct}, CPE_c, and CPE_{dl}, respectively. Due to the existence of porosity and non-uniform surface for the metallic substrates, the ideal capacitors were replaced with constant phase elements. The capacitance values of coatings (C_c) were calculated by Eq. (1), as below [23,63,64]:

$$C_c = \frac{(R_c Q_{0,c})^{\frac{1}{n}}}{R_c} \quad (1)$$

where, $Q_{0,c}$ and n are representative for the admittance of CPE_c and exponent, respectively.

Values of $|Z|_{f=0.01\ Hz}$, C_c, and frequency of breakpoint (f_b) for different coatings as a function of time are shown in Fig. 14 and Table 4. In phase diagrams, the frequency, related to the phase angle equal to

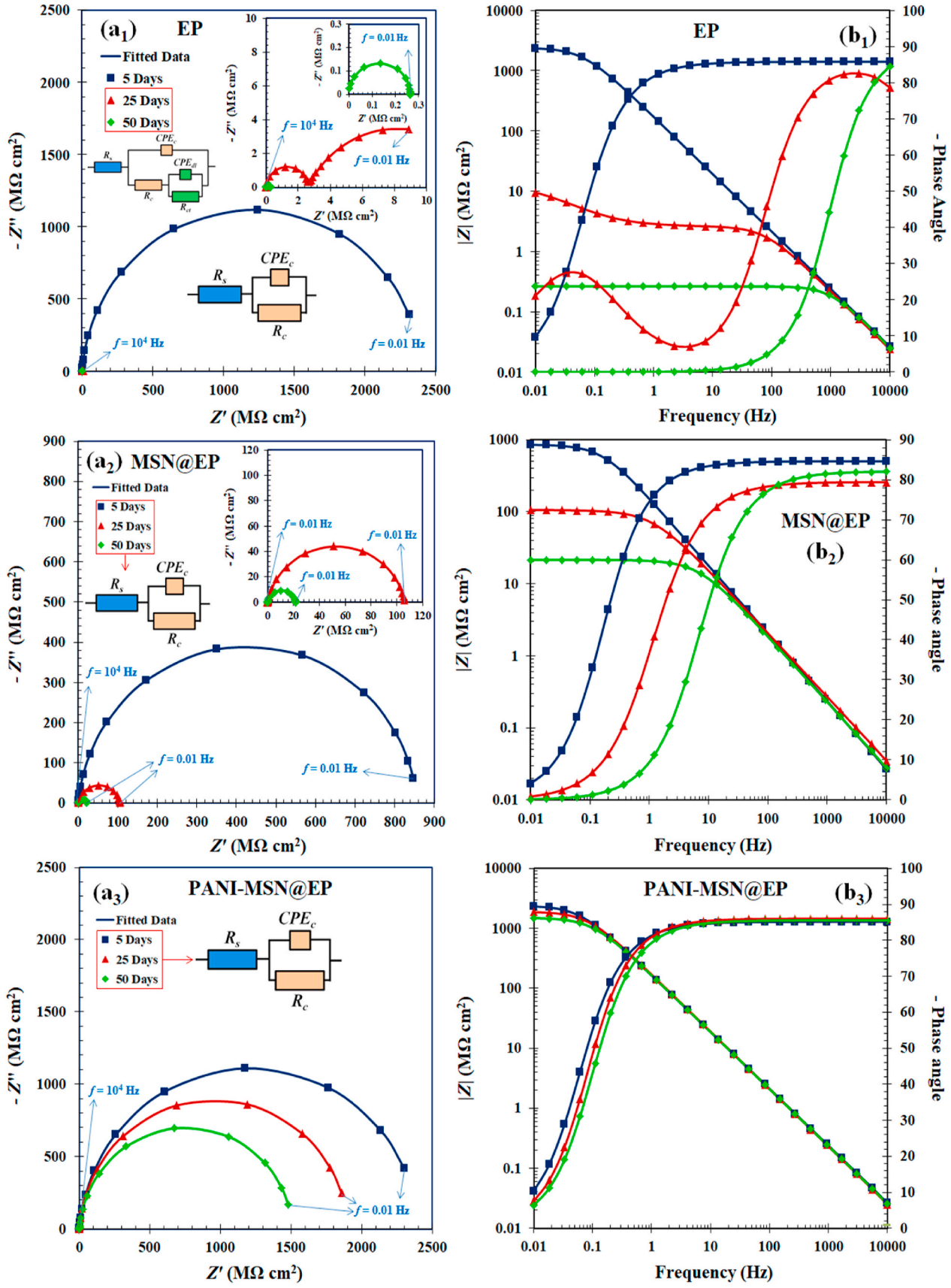

Fig. 13. Nyquist ((a_1)-(a_3)) and Bode ((b_1)-(b_3)) plots of intact epoxy coatings dipped in 3.5 wt % NaCl solution at different immersion times.

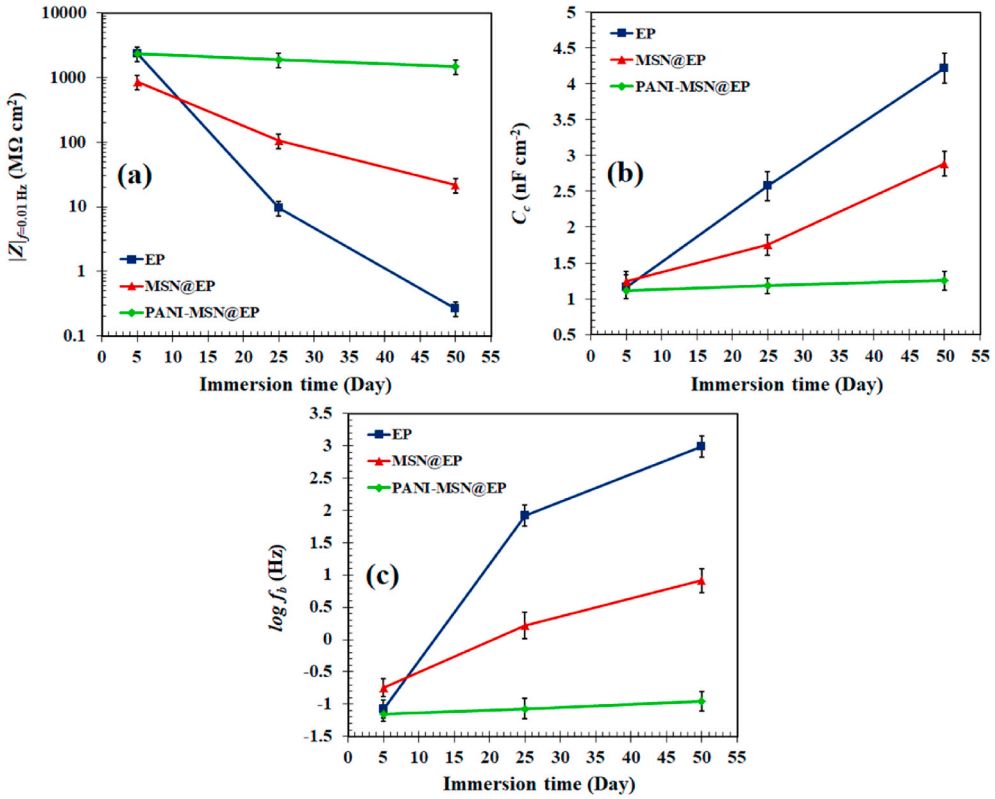

Fig. 14. $|Z|_{f=0.01\ Hz}$ (a), C_c (b), and log (f_b) (c) values of different epoxy coatings dipped in 3.5 wt % NaCl solution as a function of immersion times.

Table 4
Electrochemical parameters extracted from fitted impedance data for different coatings at various immersion times.

Sample	Immersion time (day)	R_c (MΩ cm^2)	CPE_c		R_{ct} (MΩ cm^2)	CPE_{dl}		R_t (Ω cm^2)	Log$\|Z\|_{f=0.01\ Hz}$	C_C (nF cm^{-2})	Log (f_b) (Hz)
			Y_0 (nΩ^{-1} cm^{-2} s^n)	n		Y_0 (μΩ^{-1} cm^{-2} s^n)	n				
EP											
	5	2408	1	0.85	–	–	–	2408	234	1.17	−1.07
	25	2.61	3.13	0.96	7.82	0.53	0.71	10.43	9.55	2.57	1.92
	50	0.26	5.92	0.95	0.065	88.9	0.61	0.33	0.26	4.22	2.99
MSN@EP											
	5	857.3	1.24	0.94	–	–	–	857.3	849	1.24	−0.74
	25	106.2	2.14	0.88	–	–	–	106.2	106	1.75	0.22
	50	21.55	3.69	0.91	–	–	–	21.5	21.54	2.89	0.91
PANI-MSN@EP	5	2414	1.06	0.95	–	–	–	2414	2338	1.12	−1.15
	25	1511	1.15	0.95	–	–	–	1511	1872	1.18	−1.07
	50	1906	1.21	0.96	–	–	–	1906	1488	1.25	−0.96

−45°, is considered as f_b [65]. For a coating immersed in the corrosive electrolyte, the value of f_b usually shifts to higher frequencies as a result of the electrolyte diffusion through the coating. That is why for EP coatings, the value of f_b shifted from −1.07 to 2.99 Hz after 50 days, while PANI-MSN@EP coating showed only a 16% reduction in f_b. As depicted in Figs. 13 and 14, and Table 4, $|Z|_{f=0.01\ Hz}$ for EP coating decreased from 2344 to 0.27 MΩ cm^2 after 50 days. Also, after 25 days, two-time constants were seen for EP coating, while for all nano-composite coatings, only a one-time constant can be observed for all immersion times. Decrement of $|Z|_{f=0.01\ Hz}$, shifting of f_b to higher frequencies, and increase in C_c for EP coating indicate the poor barrier properties of EP coating against the diffusion of the electrolyte and other aggressive species, such as Na^+, Cl^-, and O_2. Higher values of $|Z|_{f=0.01\ Hz}$ and observation of only one-time constant for MSN@EP and PANI-MSN@EP coatings are attributed to excellent barrier properties of MSNs and PANI-MSNs even at longer periods of immersion. In the presence of 3 wt %, $|Z|_{f=0.01\ Hz}$ values of MSN@EP and PANI-MSN@EP coatings reached 21.5 and 1488.3 MΩ cm^2 after 50 days, which are much higher than that of EP coating, indicating outstanding CPP of these coatings.

As can be seen in Fig. 14 and Table 4, after 50 days of immersion, values of C_c and $log\ f_b$ for PANI-MSN@EP coating are changed from 1.11 to 1.25 nF cm^{-2} and -1.15 to −0.96 Hz, respectively, while these values for MSN@EP coating are 2.89 nF cm^{-2} and 0.91 Hz.

An increase in values of C_c at longer immersion times can be assigned to the diffusion of the electrolyte in the coating, accumulation of corrosion products at the metal/coating interface, and the coating cathodic delamination. Better barrier properties and CPP of PANI-MSN@EP coatings can be assigned to three possible reasons. The first reason is the good dispersion of PANI-MSNs in the epoxy matrix, as discussed in detail in the RMS Section (S3), providing superior barrier properties and larger contact areas with epoxy chains and longer

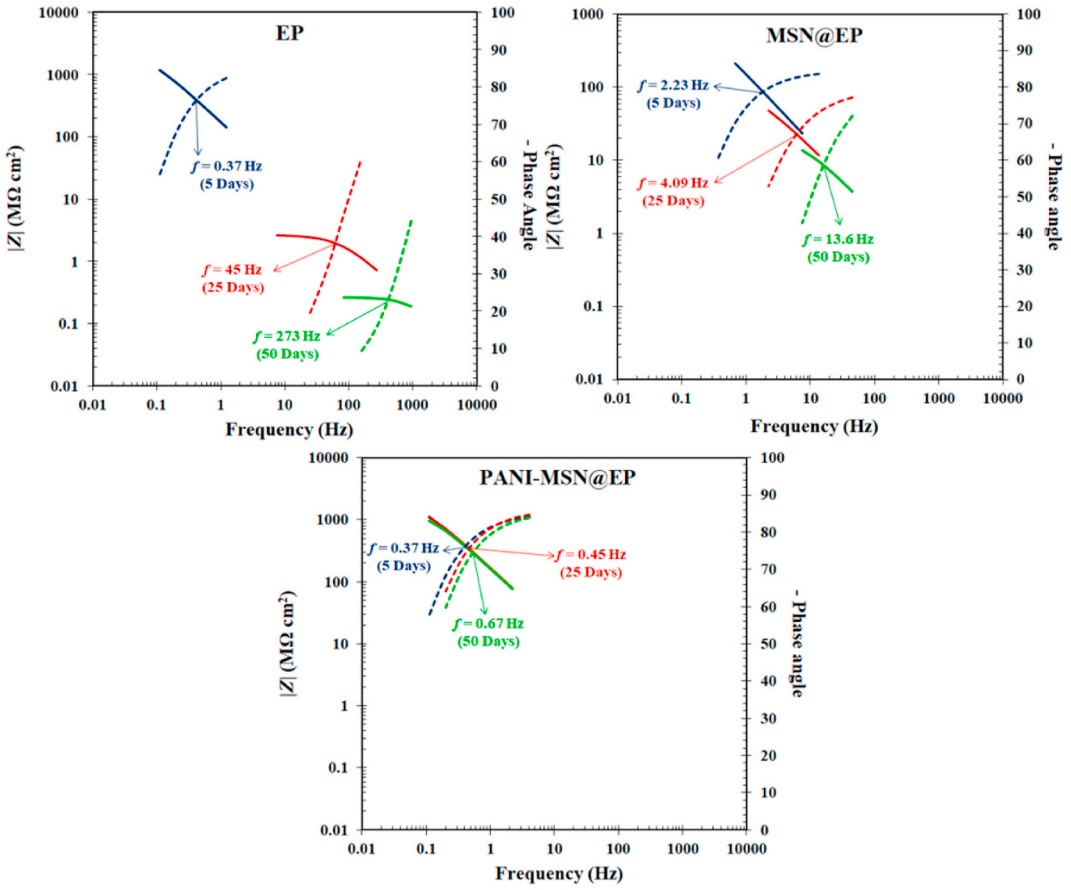

Fig. 15. IBP values of epoxy coatings dipped in 3.5 wt % NaCl solution at different immersion times.

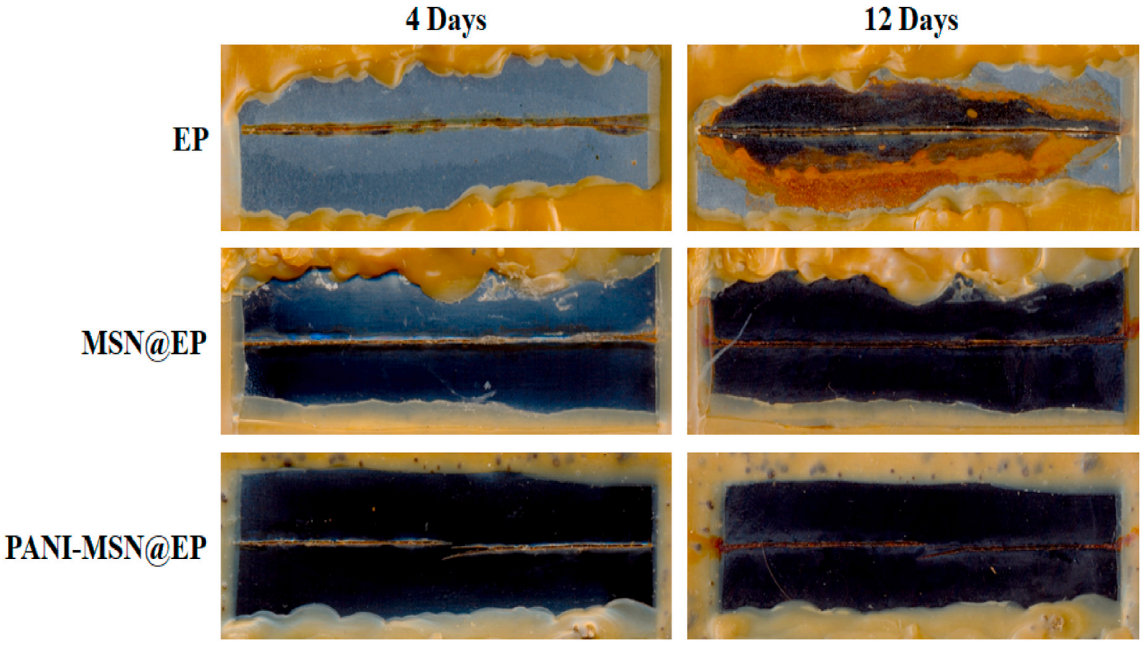

Fig. 16. The appearance of different epoxy coatings after 4 and 12 days exposure in the salt fog chamber.

tortuous path for aggressive species to pass through the coating. The second reason is the negative surface charge of MSNs and PANI, which restricts the migration of Cl^- through the matrix due to the electrostatic repulsive forces. Imperceptible release of Zn^{2+} from PANI-MSNs, as stated in detail in Section 3.2, can limit the cathodic corrosion reactions in the metal/coating interface and prolong the cathodic delamination and deterioration period of the coating.

Frequencies of intersection Bode plots (IBP) of the epoxy coatings at

different periods of immersion are presented in Fig. 15. As presented in Fig. 15, for all coatings, when the immersion time elapsed, IBP values shifted to the higher frequencies [66]. Also, EP coatings showed the highest values of IBP compared to nanocomposite coatings, indicating the higher rate of electrolyte diffusion through the coating in comparison with loaded epoxy coatings.

3.3.3. Salt spray test

To investigate visually the effectiveness of MSN and PANI-MSN nanoparticles on the CPP of epoxy coatings, the salt spray test was conducted. The appearance of different coatings after 4 and 12 days of exposure in the salt fog chamber is shown in Fig. 16. After 4 days, some rusts and corrosion products formed within the scratched region of all coatings, which is more obvious for the EP coating. Tremendous amounts of corrosion products, including different types of iron oxide/hydroxyl products, could be easily recognized in the scratch regions of EP and MSN@EP coatings after 12 days of exposure in the corrosive media. Delamination of the coating occurred for the EP coating due to the penetration of corrosive species such as (Na^+, Cl^-, and O_2) weakening the adhesion bonds between the coating and metallic substrate. Similar electrochemical behaviour is observed for the coating containing MSNs due to the lack of active inhibitive agent. Also, the formation of blisters and the detachment of coatings from substrates are accelerated by the diffusion of the corrosive electrolyte and the accumulation of corrosion products generated by anodic and cathodic corrosion reactions underneath the coatings.

As can be seen in Fig. 16, the higher CPP of PANI-MSN@EP is obvious even after 12 days and no blisters and corrosion spots are detected due to the corrosion inhibition role of Zn^{2+} cations loaded in MSNs. Once the corrosive electrolyte reaches the metal/coating interface, hydroxide ions are produced by cathodic reactions. Subsequently, the released Zn^{2+} cations can react with hydroxide groups, and eventually, the micro cathodic regions are blocked through the zinc hydroxide formation ($Zn(OH)_2$). Furthermore, PANI shells can form a passive protective layer in the scratch region with the mechanism given in Fig. 11, and provide excess corrosion protection [30,67].

4. Conclusions

Herein, MSNs cores were successfully covered with Zn^{2+} doped PANI as the shell. The influence of MSNs before and after coverage with Zn^{2+} doped PANI on the rheological, mechanical, and corrosion protection properties of the epoxy coating was studied. ICP-OES results showed the pH triggered release of Zn^{2+} in the alkaline solutions. Rheological and mechanical analyses illustrated that the coverage of MSNs with PANI enhanced the rheological properties and mechanical characteristics, i.e., yield stress and Young's modulus of the epoxy coatings. Electrochemical measurements showed that the incorporation of 3 wt % PANI-MSNs in the epoxy coating improved the active corrosion protection and barrier properties of the resulting nanocomposite coating. Modification of MSNs with PANI and doping of the nanoparticles with Zn^{2+} as an eco-friendly inorganic corrosion inhibitor were responsible for the enhanced dual active/barrier characteristics.

CRediT authorship contribution statement

Seyyed Arash Haddadi: Methodology, Writing - Original Draft, Writing - Review & Editing, Supervision, Project administration, Results Analysis, and Conceptualization. **Erfan Mehmandar:** Acquisition of data, Formal Analysis and Results Analysis. **Hossein Jabari:** Acquisition of data, Formal Analysis and Results Analysis. **Ahmad Ramazani S.A.:** Resources, Supervision. **Rahman Mohammadkhani:** Writing - Review & Editing and Results Analysis. **Ning Yan:** Writing - Review & Editing, and Conceptualization. **Mohammad Arjmand:** Methodology, Writing - Review & Editing, Resources, Supervision.

Declaration of competing interest

The authors declare that they have no known competing financial interests or personal relationships that could have appeared to influence the work reported in this paper.

Acknowledgments

The authors would like to acknowledge financial support from the University of British Columbia, Okanagan Campus, Canada. Dr. Arjmand would like to thank the financial support from the Canada Research Chairs program.

Appendix A. Supplementary data

Supplementary data related to this article can be found at https://doi.org/10.1016/j.compositesb.2021.108713.

References

[1] Liu Z, Jackson TS, Gibson J. Composition and method for inhibiting corrosion of metals. 2018.
[2] Flis J. Corrosion of metals and hydrogen-related phenomena: selected topics. Elsevier; 2016.
[3] Haddadi SA, Sa AR, Mahdavian M, Taheri P, Mol JMC, Gonzalez-Garcia Y. Self-healing epoxy nanocomposite coatings based on dual-encapsulation of nano-carbon hollow spheres with film-forming resin and curing agent. Compos B Eng 2019;175:107087.
[4] Talbot DEJ, Talbot JDR. Corrosion science and technology. CRC press; 2018.
[5] Shekari E, Khan F, Ahmed S. Economic risk analysis of pitting corrosion in process facilities. Int J Pres Ves Pip 2017;157:51–62.
[6] Koch G. Cost of corrosion. Trends oil gas Corros. Res. Technol. Elsevier; 2017. p. 3–30.
[7] Kohl M, Kalendová A, Černošková E, Bláha M, Stejskal J, Erben M. Corrosion protection by organic coatings containing polyaniline salts prepared by oxidative polymerization. J Coating Technol Res 2017;14:1397–410.
[8] Knudsen OØ, Forsgren A. Corrosion control through organic coatings. CRC Press; 2017.
[9] Pourhashem S, Rashidi AM, Jezeh MRV. Anti-corrosion nanocomposite coating. 2018.
[10] Schweitzer PA. Paint and coatings: applications and corrosion resistance. CRC press; 2005.
[11] Haddadi SA, Ramazani SA, Mahdavian M, Taheri P, Mol JMC. Mechanical and corrosion protection properties of a smart composite epoxy coating with dual-encapsulated epoxy/polyamine in carbon nanospheres. Ind Eng Chem Res 2019;58:3033–46.
[12] Nguyen-Tri P, Nguyen TA, Carriere P, Ngo Xuan C. Nanocomposite coatings: preparation, characterization, properties, and applications. Int J Corros 2018;2018.
[13] Ramezanzadeh B, Niroumandrad S, Ahmadi A, Mahdavian M, Mohamadzadeh Moghadam MH. Enhancement of barrier and corrosion protection performance of an epoxy coating through wet transfer of amino functionalized graphene oxide. Corrosion Sci 2016;103:283–304.
[14] Ammar S, Ramesh K, Vengadaesvaran B, Ramesh S, Arof AK. Amelioration of anticorrosion and hydrophobic properties of epoxy/PDMS composite coatings containing nano ZnO particles. Prog Org Coating 2016;92:54–65.
[15] Ghazizadeh A, Haddadi SA, Mahdavian M. The effect of sol-gel surface modified silver nanoparticles on the protective properties of the epoxy coating. RSC Adv 2016;6. https://doi.org/10.1039/c5ra27729a.
[16] Haddadi SA, Mahdavian M, Karimi E. Evaluation of the corrosion protection properties of an epoxy coating containing sol–gel surface modified nano-zirconia on mild steel. RSC Adv 2015;5:28769–77.
[17] Yu Y, Yeh J, Liou S, Chen C, Liaw D, Lu H. Preparation and properties of polyimide–clay nanocomposite materials for anticorrosion application. J Appl Polym Sci 2004;92:3573–82.
[18] Zea C, Barranco-García R, Chico B, Díaz I, Morcillo M, de la Fuente D. Smart mesoporous silica nanocapsules as environmentally friendly anticorrosive pigments. Int J Corros 2015;2015.
[19] Palimi MJ, Rostami M, Mahdavian M, Ramezanzadeh B. A study on the corrosion inhibition properties of silane-modified Fe2O3 nanoparticle on mild steel and its effect on the anticorrosion properties of the polyurethane coating. J Coating Technol Res 2015;12:277–92.
[20] Arash Haddadi S, Amini M, Ghaderi S, Ramazani A. Synthesis and cation-exchange behavior of expanded MoS2 nanosheets for anticorrosion applications. Mater. Today Proc 2018;5.
[21] Dias SAS, Lamaka SV, Nogueira CA, Diamantino TC, Ferreira MGS. Sol–gel coatings modified with zeolite fillers for active corrosion protection of AA2024. Corrosion Sci 2012;62:153–62.
[22] Abdullayev E, Price R, Shchukin D, Lvov Y. Halloysite tubes as nanocontainers for anticorrosion coating with benzotriazole. ACS Appl Mater Interfaces 2009;1:1437–43.

[23] Akbarzadeh S, Ramezanzadeh M, Ramezanzadeh B, Mahdavian M, Naderi R. Fabrication of highly effective polyaniline grafted carbon nanotubes to induce active protective functioning in a silane coating. Ind Eng Chem Res 2019;58:20309–22.
[24] Ramezanzadeh B, Ghasemi E, Mahdavian M, Changizi E, Mohamadzadeh Moghadam MH. Covalently-grafted graphene oxide nanosheets to improve barrier and corrosion protection properties of polyurethane coatings. Carbon N Y 2015;93:555–73.
[25] Qiu S, Li W, Zheng W, Zhao H, Wang L. Synergistic effect of polypyrrole-intercalated graphene for enhanced corrosion protection of aqueous coating in 3.5% NaCl solution. ACS Appl Mater Interfaces 2017;9:34294–304.
[26] Geim AK, Novoselov KS. The rise of graphene. Nanosci. Technol. A collect. Rev. From nat. Journals. World Scientific; 2010. p. 11–9.
[27] Liu D, Zhao W, Liu S, Cen Q, Xue Q. Comparative tribological and corrosion resistance properties of epoxy composite coatings reinforced with functionalized fullerene C60 and graphene. Surf Coating Technol 2016;286:354–64.
[28] Yeganeh M, Omidi M, Mortazavi SHH, Etemad A, Nazari MH, Marashi SM. Application of mesoporous silica as the nanocontainer of corrosion inhibitor. Corros. Prot. Nanoscale 2020:275–94 [Elsevier].
[29] Saremi M, Yeganeh M. Application of mesoporous silica nanocontainers as smart host of corrosion inhibitor in polypyrrole coatings. Corrosion Sci 2014;86:159–70.
[30] Ramezanzadeh B, Bahlakeh G, Ramezanzadeh M. Polyaniline-cerium oxide (PAni-CeO2) coated graphene oxide for enhancement of epoxy coating corrosion protection performance on mild steel. Corrosion Sci 2018;137:111–26.
[31] Kartsonakis IA, Danilidis IL, Pappas GS, Kordas GC. Encapsulation and release of corrosion inhibitors into titania nanocontainers. J Nanosci Nanotechnol 2010;10:5912–20.
[32] Shchukina E, Shchukin D, Grigoriev D. Effect of inhibitor-loaded halloysites and mesoporous silica nanocontainers on corrosion protection of powder coatings. Prog Org Coating 2017;102:60–5.
[33] Shchukin DG, Möhwald H. Surface-engineered nanocontainers for entrapment of corrosion inhibitors. Adv Funct Mater 2007;17:1451–8.
[34] Haddadi SA, Ramazani SAA, Mahdavian M, Taheri P, Mol JMC. Fabrication and characterization of graphene-based carbon hollow spheres for encapsulation of organic corrosion inhibitors. Chem Eng J 2018;352.
[35] Pirhady Tavandashti N, Ghorbani M, Shojaei A, Gonzalez-Garcia Y, Terryn H, Mol JMC. PH responsive Ce(III) loaded polyaniline nanofibers for self-healing corrosion protection of AA2024-T3. Prog Org Coating 2016;99:197–209.
[36] Montemor MF. Functional and smart coatings for corrosion protection: a review of recent advances. Surf Coating Technol 2014;258:17–37.
[37] Kopeć M, Szczepanowicz K, Mordarski G, Podgórna K, Socha RP, Nowak P, et al. Self-healing epoxy coatings loaded with inhibitor-containing polyelectrolyte nanocapsules. Prog Org Coating 2015;84:97–106.
[38] Izadi M, Shahrabi T, Ramezanzadeh B. Synthesis and characterization of an advanced layer-by-layer assembled Fe3O4/polyaniline nanoreservoir filled with Nettle extract as a green corrosion protective system. J Ind Eng Chem 2018;57:263–74.
[39] Yeganeh M, Asadi N, Omidi M, Mahdavian M. An investigation on the corrosion behavior of the epoxy coating embedded with mesoporous silica nanocontainer loaded by sulfamethazine inhibitor. Prog Org Coating 2019;128:75–81.
[40] Chang M, Cao XL, Zeng H, Zhang L. Enhancement of the ultraviolet emission of ZnO nanostructures by polyaniline modification. Chem Phys Lett 2007;446:370–3.
[41] Li X, Chen W, Bian C, He J, Xu N, Xue G. Surface modification of TiO2 nanoparticles by polyaniline. Appl Surf Sci 2003;217:16–22.
[42] Amrollahi S, Ramezanzadeh B, Yari H, Ramezanzadeh M, Mahdavian M. Synthesis of polyaniline-modified graphene oxide for obtaining a high performance epoxy nanocomposite film with excellent UV blocking/anti-oxidant/anti-corrosion capabilities. Compos B Eng 2019;173:106804.
[43] Shchukin DG, Zheludkevich M, Yasakau K, Lamaka S, Ferreira MGS, Möhwald H. Layer-by-Layer assembled nanocontainers for self-healing corrosion protection. Adv Mater 2006;18:1672–8.
[44] Taheri NN, Ramezanzadeh B, Mahdavian M, Bahlakeh G. In-situ synthesis of Zn doped polyaniline on graphene oxide for inhibition of mild steel corrosion in 3.5 wt.% chloride solution. J Ind Eng Chem 2018;63:322–39.
[45] Narayan R, Nayak UY, Raichur AM, Garg S. Mesoporous silica nanoparticles: a comprehensive review on synthesis and recent advances. Pharmaceutics 2018;10:118.
[46] Stöber W, Fink A, Bohn E. Controlled growth of monodisperse silica spheres in the micron size range. J Colloid Interface Sci 1968;26:62–9.
[47] Li W, Yue Q, Deng Y, Zhao D. Ordered mesoporous materials based on interfacial assembly and engineering. Adv Mater 2013;25:5129–52.
[48] Thommes M, Kaneko K, Neimark AV, Olivier JP, Rodriguez-Reinoso F, Rouquerol J, et al. Physisorption of gases, with special reference to the evaluation of surface area and pore size distribution (IUPAC Technical Report). Pure Appl Chem 2015;87:1051–69.
[49] Lin-Vien D, Colthup NB, Fateley WG, Grasselli JG. The handbook of infrared and Raman characteristic frequencies of organic molecules. Elsevier; 1991.
[50] Campos M, Miziara TAS, Cristovan FH, Pereira EC. Investigations of the electrical conduction mechanisms of polyaniline-DBSA/poly (acrylonitrile-butadiene styrene) blends. J Appl Polym Sci 2014;131.
[51] Pavia DL. Introduction to spectroscopy. CengageBrain. com; 2009.
[52] Cendrowski K, Chen X, Zielinska B, Kalenczuk RJ, Rümmeli MH, Büchner B, et al. Synthesis, characterization, and photocatalytic properties of core/shell mesoporous silica nanospheres supporting nanocrystalline titania. J Nanoparticle Res 2011;13:5899–908.
[53] Shakoor A, Rizvi TZ, Nawaz A. Raman spectroscopy and AC conductivity of polyaniline montmorillonite (PANI–MMT) nanocomposites. J Mater Sci Mater Electron 2011;22:1076–80.
[54] Abdullah HS. Electrochemical polymerization and Raman study of polypyrrole and polyaniline thin films. Int J Phys Sci 2012;7:5468–76.
[55] Zulfiqar U, Subhani T, Husain SW. Synthesis and characterization of silica nanoparticles from clay. J Asian Ceram Soc 2016;4:91–6.
[56] Taheri NN, Ramezanzadeh B, Mahdavian M. Application of layer-by-layer assembled graphene oxide nanosheets/polyaniline/zinc cations for construction of an effective epoxy coating anti-corrosion system. J Alloys Compd 2019;800:532–49.
[57] Mostafaei A, Zolriasatein A. Synthesis and characterization of conducting polyaniline nanocomposites containing ZnO nanorods. Prog Nat Sci Mater Int 2012;22:273–80.
[58] Zaccariello G, Moretti E, Storaro L, Riello P, Canton P, Gombac V, et al. TiO2–mesoporous silica nanocomposites: cooperative effect in the photocatalytic degradation of dyes and drugs. RSC Adv 2014;4:37826–37.
[59] Hwang J, Pyo M. pH-dependent mass and volume changes of polypyrrole/poly (styrene sulfonate). Bull Chem Soc 2006;27:2067.
[60] Sapurina IY, Shishov MA. Oxidative polymerization of aniline: molecular synthesis of polyaniline and the formation of supramolecular structures. New Polym Spec Appl 2012;740:272.
[61] Pirhady Tavandashti N, Ghorbani M, Shojaei A, Mol JMC, Terryn H, Baert K, et al. Inhibitor-loaded conducting polymer capsules for active corrosion protection of coating defects. Corrosion Sci 2016;112:138–49.
[62] Tian Z, Yu H, Wang L, Saleem M, Ren F, Ren P, et al. Recent progress in the preparation of polyaniline nanostructures and their applications in anticorrosive coatings. RSC Adv 2014;4:28195–208.
[63] Hirschorn B, Orazem ME, Tribollet B, Vivier V, Frateur I, Musiani M. Determination of effective capacitance and film thickness from constant-phase-element parameters. Electrochim Acta 2010;55:6218–27.
[64] Haddadi SA, Ghaderi S, Sadeghi M, Gorji B, Ahmadijokani F, Sa AR, et al. Enhanced active/barrier corrosion protective properties of epoxy coatings containing eco-friendly green inorganic/organic hybrid pigments based on zinc cations/Ferula Asafoetida leaves. J Mol Liq 2020:114584.
[65] Hack HP, Scully JR. Defect area determination of organic coated steels in seawater using the breakpoint frequency method. J Electrochem Soc 1991;138:33.
[66] Xu A, Zhang F, Jin F, Zhang R, Luo B, Zhang T. The evaluation of coating performance by analyzing the intersection of bode plots. Int J Electrochem Sci 2014;9:5116–25.
[67] Hayatgheib Y, Ramezanzadeh B, Kardar P, Mahdavian M. A comparative study on fabrication of a highly effective corrosion protective system based on graphene oxide-polyaniline nanofibers/epoxy composite. Corrosion Sci 2018;133:358–73.